Tailoring of magnetism & electron transport of manganate thin films by controlling the Mn–O–Mn bond angles via strain engineering

P. Henning, Robert Gruhl, U. Ross, V. Roddatis, V. Bruchmann-Bamberg, K. P. Stroh, M. Seibt, Philipp Gegenwart, V. Moshnyaga

Angaben zur Veröffentlichung / Publication details:

Henning, P., Robert Gruhl, U. Ross, V. Roddatis, V. Bruchmann-Bamberg, K. P. Stroh, M. Seibt, Philipp Gegenwart, and V. Moshnyaga. 2024. "Tailoring of magnetism & electron transport of manganate thin films by controlling the Mn–O–Mn bond angles via strain engineering." *Scientific Reports* 14 (1): 3253. https://doi.org/10.1038/s41598-024-53722-9.

scientific reports

Check for updates

OPEN

Tailoring of magnetism & electron transport of manganate thin films by controlling the Mn–O–Mn bond angles via strain engineering

P. Henning[1], R. Gruhl[2], U. Ross[3], V. Roddatis[4], V. Bruchmann-Bamberg[1], K. P. Stroh[1], M. Seibt[3], P. Gegenwart[2] & V. Moshnyaga[1]✉

Strain engineering beyond substrate limitation of colossal magnetoresistant thin $(La_{0.6}Pr_{0.4})_{0.7}Ca_{0.3}MnO_3$ (LPCMO) films on $LaAlO_3$-buffered $SrTiO_3$ (LAO/STO) substrates has been demonstrated using metalorganic aerosol deposition technique. By growing partially relaxed 7–27 nm thick heteroepitaxial LAO buffer layers on STO a perfect lattice matching to the LPCMO has been achieved. As a result, strain-free heteroepitaxial 10–20 nm thick LPCMO/LAO/STO films with bulk-like ferromagnetic metallic ground state were obtained. Without buffer the coherently strained thin LPCMO/STO and LPCMO/LAO films were insulating and weakly magnetic. The reason for the optimized magnetotransport in strain-free LPCMO films was found to be a large octahedral Mn–O–Mn bond angle φ_{OOR} ~ 166–168° as compared to the significantly smaller one of φ_{OOR} ~ 152–156° determined for the tensile (LPCMO/STO) and compressively (LPCMO/LAO) strained films.

Heteroepitaxial growth of complex oxide films with perovskite structure, i.e., cuprates, manganites, cobaltates, nickelates, etc., has been considered to be a challenging task because of two important issues. *First*, the practically unavoidable lattice misfit between the film and substrate strongly limits the choice for a suitable substrate and leads to a biaxial "epitaxy stress". The latter is added to the intrinsic chemical pressure solely determined by the cation stoichiometry and tolerance factor[1,2] of, e.g., optimally doped $(La_{1-y}Pr_y)_{0.7}Ca_{0.3}MnO_3$ (LPCMO)[3]. *Second*, due to the inherent coupling of electron, spin and lattice degrees of freedom[4–6] the electronic properties of the heteroepitaxial films are strongly influenced by epitaxy stress. This usually leads to a degradation of the electronic properties of thin manganite films.[7,8] It can be theorized that thin heteroepitaxial films of LPCMO, which is known as a prototypic colossal magnetoresistive[9] manganite, are particularly sensitive to strain effects. Being a bandwidth- controlled manganite with increased orthorhombic distortion[10] and enhanced electron–phonon coupling[11], the LPCMO properties are easily influenced by lattice strain and disorder. Thus, to investigate intrinsic electron–phonon and spin-phonon interactions, e.g. controlling ultrafast reflectivity and magnetization dynamics[12] as well as thermal conductivity[13], stress-free thin heteroepitaxial LPCMO films are necessary.

Stress-free heteroepitaxial manganite films can be obtained by a trivial increase of their thickness to exceed the critical thickness which usually amounts to $d_c \sim 60–150$ nm[14,15] and depends strongly on the film/substrate lattice misfit. Remarkably, strain relaxation in some cases has been found to be incomplete even for very thick films, $d \sim 300\ nm >> d_c$[15]. This often involves the formation of oxygen vacancies[16] as well as changes in the cation stoichiometry, both degrading the film properties. Another possibility is provided by the so called *domain matching epitaxy*[17] known to take place for extremely large values of film/substrate lattice misfit $\varepsilon > 7–8\%$, which is the case for e.g. manganite films grown on MgO substrates[18,19]. The stress relaxation occurs via introduction of misfit dislocations at the film/substrate interface. However, in this case the bulk-like electromagnetic properties, e.g., ferromagnetism and metal–insulator transition for optimally doped LPCMO and $La_{0.7}Ca_{0.3}MnO_3$ (LCMO) films, can also only be observed for relatively thick films with $d \approx 100$ nm[18,19]. The magnetotransport properties of thinner and seemingly relaxed LPCMO/MgO films with $d = 10–20$ nm, are strongly influenced by residual

[1]Erstes Physikalisches Institut, Georg-August-Universität Göttingen, Friedrich-Hund-Platz 1, 37077 Göttingen, Germany. [2]Experimentalphysik VI, Center for Electronic Correlations and Magnetism, University of Augsburg, 86159 Augsburg, Germany. [3]4th Institute of Physics – Solids and Nanostructures, Georg-August-Universität Göttingen, Friedrich-Hund-Platz 1, 37077 Göttingen, Germany. [4]GFZ German Research Centre for Geosciences, Helmholtz Centre Potsdam, Telegrafenberg, 14473 Potsdam, Germany. ✉email: vmosnea@gwdg.de

lattice strain and cation disorder, induced by misfit dislocations. As a result, such optimally doped films reveal a strongly suppressed magnetism in addition to insulating behavior.

The established strong strain-driven effects have also sparked the idea to employ *strain engineering* as a tool for tuning the functional properties of perovskite films.[20,21] In principle, this can be achieved through the use of suitable buffer layers, which also need to be obtained in the relaxed state. Namely, they must be thick enough $d > 100$ nm to enable a perfect lattice matching as was shown earlier for lightly doped La_2CuO_4[22], high-T_C superconducting $La_{2-x}Sr_xCuO_4/SrLaAlO_4/SrTiO_3$ (STO)[23] and $GdBa_2Cu_3O_{7-x}/La_{0.7}Sr_{0.3}MnO_3/LaAlO_3$[24] films. This approach appears generically similar to the search for a suitable substrate, the choice of which, however, is very limited for an arbitrary chosen film composition. Even for almost perfect lattice matching, e.g., for LCMO films grown on $NdGaO_3$ (NGO) substrate, the octahedral coupling between the film and the substrate, having different octahedral tilt and rotation patterns, was shown to strongly influence the structure and properties of LCMO/NGO heteroepitaxial films[25–27]. Furthermore, the octahedral tilt/rotation angle φ_{OOR} is a well-known structural parameter controlling the structure and electronic properties of perovskite manganites[28]. It has also been considered as an important target parameter for the strain engineering of thin perovskite manganite films in order to optimize their properties[29–32].

Recently, a fundamentally different approach, namely, the strain engineering beyond substrate limitations[33–36], has been suggested in order to optimize structure and electronic properties of heteroepitaxial films. It is based on thickness tuning of a heteroepitaxially grown and partially relaxed buffer layer to achieve a controllable strain state of the subsequently grown complex oxide film. For example, by using a $Sr_3Al_2O_6$ (SAO) buffer layer with the thickness of $d_{SAO} \leq 5$ nm grown on STO(100) substrate, the strain in a $Nd_{0.5}Sr_{0.5}MnO_3$ (NSMO) can be controlled up to ≈ 1% by gradual strain relaxation of the SAO buffer[34]. However, this attempt, although resulting in the relaxed NSMO film, unexpectedly, did not lead to the recovery of the intrinsically complex magnetic, electric and structural NSMO bulk behavior. Namely, the coupled ferromagnetic/anti-ferromagnetic-charge ordered and structural phase transitions around 150 K, both inherent to the bulk NSMO[37], have not been detected in the strain-free NSMO/SLAO/STO film. A promising approach to strain engineering beyond substrate limitations has been reported by Deng et al.[35] They demonstrated that the insertion of a $Ca_{0.96}Ce_{0.04}MnO_3$ (CCMO) buffer layer with a thickness $d_{CCMO} = 2–9$ nm between a $BiFeO_3$ (BFO) film and the LAO, LSAT, STO, and $NdScO_3$ substrates allows one to create the desired strain state in the BFO film. As a result, a metastable tetragonal-like phase in BFO films as well as the rhombohedral-tetragonal phase transition have been demonstrated. A room temperature electrical switching in BFO-based heterostructures was realized. Finally, by using a $CaMnO_3$ (CMO) buffer layer with $d_{CMO} = 10$ nm grown on STO(100), c-axis oriented Ruddlesden-Popper $Pr_{0.5}Ca_{1.5}MnO_4$ (RP-PCMO) films with bulk structure and high charge order transition temperature $T_{CO} \approx 320$ K were obtained[36]. A partially relaxed CMO buffer enables the bridging of a very large RP-PCMO/STO lattice misfit of about 3%. Note, that without CMO buffer the RP-PCMO films did not show c-axis orientation but rather an a-axis orientation.

Here we report the successful strain engineering of $(La_{0.6}Pr_{0.4})_{0.7}Ca_{0.3}MnO_3$ (LPCMO) films grown on STO(100) substrates by using ultrathin LAO buffer layers. Cubic STO with lattice constant $a = 0.3905$ nm is a standard substrate for manganite films. The LAO/STO epitaxy pair is a prominent 2DEG system[38], for which very thin films of rhombohedral LAO with pseudocubic lattice parameter $a_{LAO} = 0.379$ nm and high structural quality are known to grow epitaxially on STO. Considering a large lattice LAO/STO misfit of 3% one can suppose a partial strain relaxation and, thus, an in-plane LAO lattice constant approaching that of LPCMO ($a = 0.385–0.386$ nm[19]) already for a very thin LAO buffer. Indeed, by tuning the LAO thickness in the range of $d_{LAO} = 3–10$ nm, very thin $d \approx 10–20$ nm and stress-free heteroepitaxial LPCMO/LAO/STO(100) films with a bulk-like magnetotransport have been prepared. In contrast, the ferromagnetic metallic behavior was suppressed in coherently tensile strained LPCMO/STO(100) films. Furthermore, we show that the structural mechanism behind the strain-induced degradation in thin LPCMO/STO(100) films is a tetragonal distortion, accompanied by a strong decrease of octahedral tilt/rotation Mn–O–Mn angle down to $\varphi_{OOR} \approx 156°$. Meanwhile, the strain-free LPCMO/LAO/STO film possess a much larger $\varphi_{OOR} \approx 166°$, which favors the ferromagnetic metallic ground state of LPCMO.

Experimental details

LPCMO and LAO films have been prepared by means of metalorganic aerosol deposition (MAD) technique[19,39], based on spraying precursor solutions, i.e., La-, Pr-, Ca-, Mn-, and La- and Al-acetylacetonates in dimetylformamide, onto a heated substrate. Precursors taken in empirically determined molar ratios, e.g. (La + Pr + Ca)/Mn = 1.35 and La/Al = 1.2 provide the required film stoichiometry. This was further evidenced by an almost perfect surface morphology and microstructure of the films addressed in details below. STO(100), LAO(100) and MgO(200) substrates were purchased from Crystal GmbH; the STO substrates were TiO_2-terminated[39] prior to deposition. The films have been grown in ambient atmosphere ($pO_2 = 0.2$ bar) at a substrate temperature $T_{sub} = 900–950$ °C under growth rate of $v \approx 0.3$ nm/s. After deposition the films were cooled down to room temperature withiin 15 min.

Structure and thickness of the prepared films were characterized by X-ray diffraction (XRD) in Θ-2Θ Bragg–Brentano geometry and by small angle X-ray reflection (XRR) with Cu–K_α radiation using a Bruker "D8" diffractometer. In-plane epitaxy was characterized by reciprocal space mapping measured using a "Malvern Panalytical Empyrean" diffractometer. Surface morphology of the films has been visualized by atomic force microcopy (AFM) from "Bruker Innova". Scanning Transmission Electron microscopy (STEM) was performed using a "Thermo Fisher Scientific" (TFS) Themis Z 80-300 (S)TEM operated at 300 kV, and equipped with a TFS SuperX Energy Dispersive X-ray (EDX) detector, and a Gatan Imaging Filter (GIF) Continuum 1065. The microscope was tuned for a sub-Angstrom resolution with a beam convergence angle of 21.4 mrad. Specimens for STEM were prepared with a lift-out Focused Ion Beam technique using a TFS Helios G4UC dual beam

instrument. TEM lamellas were prepared along the [100] and [110] directions using a TFS Helios UC focused ion beam instrument with a beam energy of 30 kV; a final cleaning step was carried out at low energy (2 kV). The magnetic and electric properties were measured using a SQUID magnetometer (MPMS XL) and a Physical Property Measurements System (PPMS), respectively, from "Quantum Design".

Results

As a first step, magnetism and electron transport of thin (d = 16–20 nm) LPCMO films, heteroepitaxially grown on LAO, STO and MgO substrates by MAD technique, were studied. The films on STO and LAO show atomically smooth AFM surface morphology (see Supplemental Material[41], Fig. SM-1), evidencing the layer-by-layer (step-flow) growth mode; the estimated mean square roughness was RMS = 0.2–0.4 nm. According to the XRD data (see Fig. SM-2a,b, ref.[40]) the LPCMO films, grown directly on STO and LAO substrates, display out-of-plane c-lattice parameters of $c_{STO} = 0.3796$ nm and $c_{LAO} = 0.3948$ nm, indicating a coherent tensile $\varepsilon_{STO} = 1.7\%$ and compressive $\varepsilon_{LAO} = -2.2\%$ stress, respectively. In contrast, the LPCMO film heteroepitaxially grown on MgO possesses a c-lattice parameter of $c_{MgO} = 0.3863$ nm (see Fig. SM-2c, ref.[41]), which is very close to the bulk LPCMO[3,9], indicating a stress-free state in agreement with earlier observations[19].

In Fig. 1 we present the temperature dependences of magnetization (1a), 1b)) and resistivity (1c)) for thin LPCMO films grown on different substrates. One can see that the strained films on STO and LAO, independent of the sign of strain, are weakly magnetic and show insulating behavior. This is in clear contrast with the known bulk behavior of LPCMO with coupled ferromagnetic and metal–insulator transitions at $T_C = T_{MI} \approx 200$ K[19]. Interestingly, the 16 nm thick film on MgO, being in the overall stress-free state, shows a similar insulating behavior and totally suppressed magnetism. In Fig. 1a one can see only a weak paramagnetic contribution most likely originated from magnetic impurities in the MgO substrate. Remarkably, the bulk-like ferromagnetic metallic behavior has been recovered in a 20 nm thick LPCMO film by introducing a 10 nm thick LAO buffer layer. The bulk-like behavior can also be achieved in an LPCMO/MgO film by increasing its thickness up to 70 nm. In both cases (see Fig. 1) distinct coupled phase transitions can be seen both in the M(T) and ρ(T) curves at a temperature $T_C = T_{MI} \approx 194$ K. Considering the films on MgO substrate, a recovering of the phase transition and the bulk-like behavior in a strain-free thicker LPCMO film is intimately linked to the reduction of lattice strain and disorder effects caused by misfit dislocations. In other words, the critical thickness of disordered films on MgO measures at least $d_0 \sim 16$ nm. Hence, the observation of bulk-like magnetotransport behavior in 20 nm thick LPCMO/LAO/STO film hints to its stress-free state as well as to the absence/diminishing of the disorder at the LPCMO/LAO interface.

To study the influence of the LAO buffer thickness on the elastic decoupling between the LPCMO film and STO substrate we have systematically changed the LAO thickness in the range of $d_{LAO} = 0$–27 nm. The corresponding results of temperature-dependent magnetic and resistive measurements are also shown in Fig. 1. One can see in Fig. 1a and b that the introduction of an merely 2.5 nm thick LAO buffer drastically changes the magnetotransport: an FM transition with $T_C = 175$ K as well as an MI-like transition with $T_{MI} \approx 80$–90 K (see Fig. 1b)

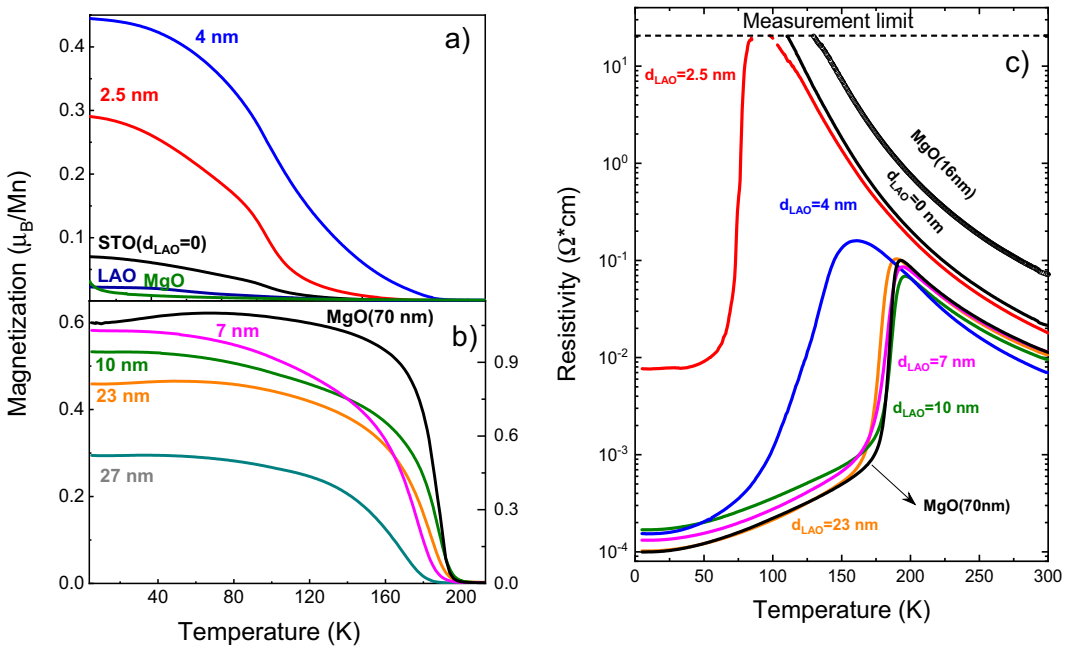

Figure 1. Temperature dependences of: magnetic moment (**a**, **b**) and electrical resistivity (**c**) for thin LPCMO films on STO, LAO and MgO substrates as well as for LPCMO(20 nm)/LAO(d)/STO(100) films with different thickness of LAO buffer layer, $d_{LAO} = 0$–27 nm. In (**c**) the points between 80 and 100 K for $d_{LAO} = 2.5$ nm sample are missing because the resistivity exceeds the measurement limit $2*10^1$ Ω*cm.

were detected. By further increasing the LAO thickness both T_C and T_{MI} were found to progressively increase and for $d_{LAO} \geq 7$ nm a bulk-like LPCMO magnetotransport has been obtained. Interestingly, for $0 < d_{LAO} \leq 7$ nm the LPCMO films show a complex magnetic behavior with two distinct phase transitions determined from the temperature coefficient of magnetization TCM = 100%(1/M)(dM/dT), shown in Fig. SM-3[41]. Namely, a low $T_{C1} = 105–110$ K and a high $T_{C2} \approx 136–200$ K magnetic phases can be deduced. Note, that T_{C1}, being almost constant and close to the temperature of structural phase transition in STO at 105 K[42], likely indicates the presence of an interfacial magnetic phase at the LPCMO/LAO interface; it may still be elastically coupled to the STO substrate for very thin ($d_{LAO} < 7$ nm) LAO buffer layers. The Curie temperature T_{C2} increases progressively with increasing the LAO thickness in the range of $0 < d_{LAO} < 7$ nm and then saturates for $7 \leq d_{LAO} \leq 23$ nm, displaying values close to the Curie temperatures of bulk LPCMO $T_C = 195–200$ K. The electrical resistivity behaves similarly (see Fig. 1c) showing ρ(T) curves with a pronounced MI transition at $T_{MI} = 190–200$ K ≈ T_C and relatively low residual resistivity $\rho(5K) \approx 10^{-4}$ Ωcm for 20 nm thick LPCMO films grown on LAO buffer with thicknesses $7 \leq d_{LAO} \leq 23$ nm.

To quantify the strain effect in thin LPCMO films we studied the in-plane and out-of-plane epitaxy of the grown LPCMO/LAO(d_{LAO})/STO heterostructures using reciprocal space mapping (RSM) and X-ray diffraction (XRD), respectively. In Fig. 2a,b and c the RSM patterns of three representative samples with $d_{LAO} = 0$, 4 and 10 nm are presented, respectively. The RSM of a strain-free 70 nm thick LPCMO/MgO film is also shown in Fig. 2c for comparison. One can see that the LPCMO/STO film ($d_{LAO} = 0$) is coherently strained as LPCMO and STO possess the same in-plane lattice parameter, $a_{LPCMO} = a_{STO} = 0.3905$ nm. Correspondingly, the out-of-plane c-lattice parameter, estimated from both RSM (Fig. 2a) and XRD (see Fig. SM-2a, ref.[41]) is significantly reduced: $c_{LPCMO} \approx 0.380$ nm. For the very thin buffer layer $d_{LAO} = 4$ nm (see Fig. 2b) a relaxation of the LPCMO film, accompanied by an increase of its out-of-plane lattice parameter up to $c_{LPCMO} \approx 0.382$ nm can be recognized. However, it remains smaller than the pseudo-cubic lattice parameter of the completely relaxed LPCMO/MgO film, c = 0.3863 nm, observed in the corresponding RSM (see Fig. 2d) and XRD (Fig. SM-2b) patterns. The intensity of the XRD peak of the 4 nm thick LAO buffer is too weak to obtain a reliable quantitative estimate, but nevertheless a tendency to the LAO relaxation can be deduced from the RSM pattern in Fig. 2b. Finally, in

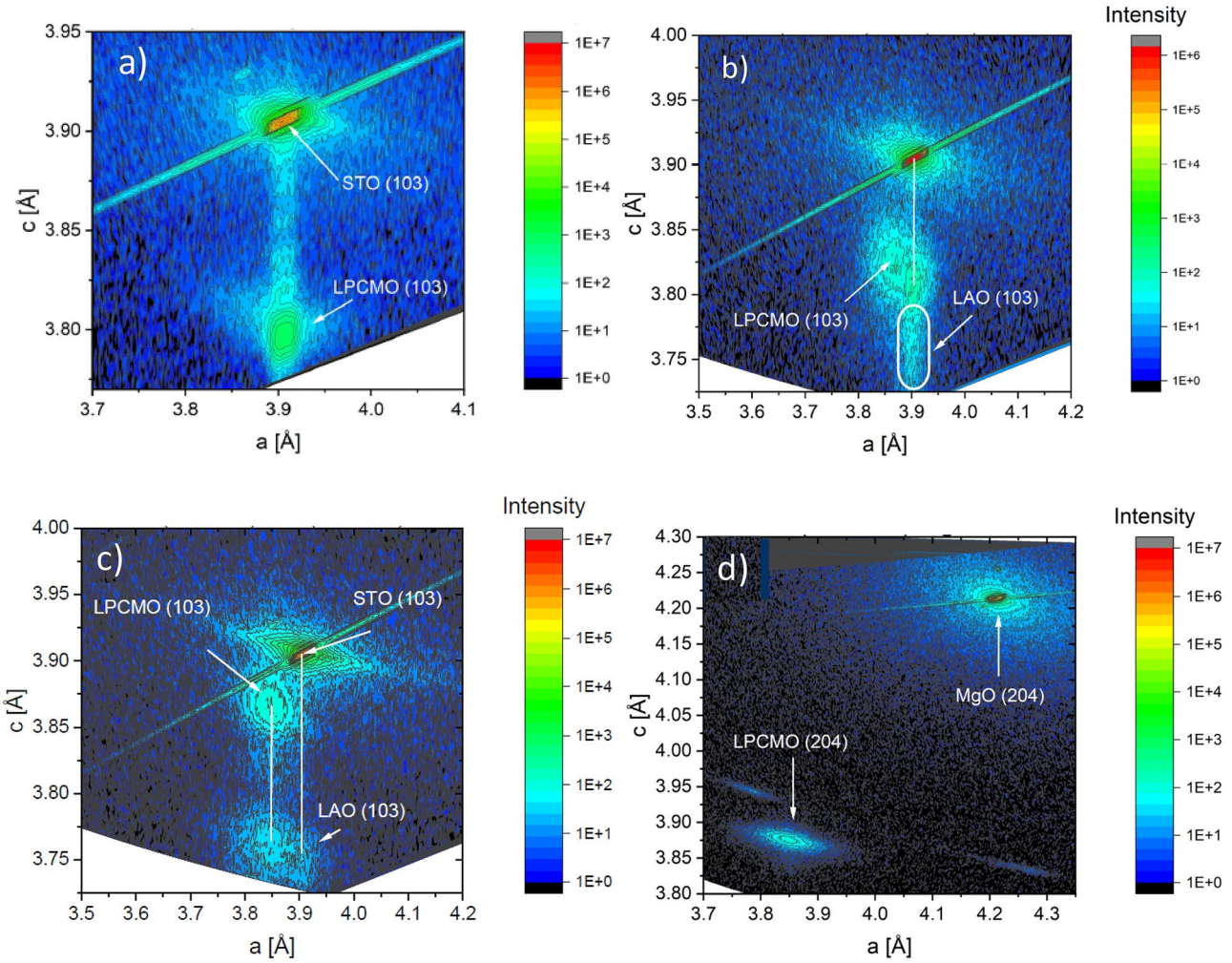

Figure 2. Reciprocal space mapping of: (**a**) LPCMO(30nm)/STO(100); (**b**) LPCMO(20 nm)/LAO(4 nm)/STO; (**c**) LPCMO(20nm)/LAO(10 nm)/STO and (**d**) LPCMO(70nm)/MgO films.

the sample with $d_{LAO} = 10$ nm (Fig. 2c) the LPCMO shows in- and out-of-plane lattice parameters which are very close to the corresponding bulk values, i.e., $c_{LPCMO} \sim a_{LPCMO} \approx 0.386$ nm[9]. Moreover, the LPCMO is epitaxially grown on the LAO buffer as they both share almost the same in-plane lattice constant. In addition, the LAO buffer appears to be tetragonally distorted since its out-of-plane parameter $c_{LAO} = 0.377$ nm is still smaller and the in-plane parameter is significantly larger $a_{LAO} \sim 0.385$ nm than the bulk value $c_{LAO} = 0.379$ nm.

An interesting observation can be made in Fig. SM-2e,f[41], where the XRD patterns for the LAO/STO buffer film have been measured before and after LPCMO deposition. One can see that the c-axis lattice constant of LAO buffer layers with thickness $d_{LAO} = 10$ and 20 nm shows an increase from $c \sim 0.375$ and 0.376 nm up to $c \sim 0.377$ nm after deposition of 20 nm thick LPCMO film. This indicates that the mechanism underlying the elastic film-buffer interaction includes a mutual adjustment of LAO and LPCMO lattices at the heteroepitaxial LPCMO/LAO interface thereby reducing its elastic energy. Being a general property of all epitaxial film/substrate interfaces, such adjustment leading to the increase of the c-lattice parameter of the LAO buffer becomes clearly visible since both LAO buffer and LPCMO film are of comparable thicknesses ~ 10–20 nm. Thus, we can draw two important conclusions: (1) thin LPCMO films are heteroepitaxially grown on the LAO/STO films and (2) the stress in the LPCMO films is controlled by the thickness of the LAO buffer, yielding almost complete stress relaxation for $7 < d_{LAO} < 20$ nm.

In Fig. 3 we summarized the RSM/XRD results and the measured T_C values of LPCMO for all samples with different thicknesses of the LAO buffer layers studied here. One can see that for the coherently tensile strained ($\varepsilon = -1.7\%$) film on STO substrate ($d_{LAO} = 0$ nm) and the compressively strained film on LAO substrate ($d_{LAO} \rightarrow \infty$) with $\varepsilon = +2.2\%$ both ferromagnetism and metallicity are suppressed and the ground state of LPCMO seems to be FM insulating with $T_C(STO) \approx 136$ K and $T_C(LAO) \approx 64$ K. The thickness of the LAO buffer does play a decisive role in controlling magnetotransport and leads to a bulk-like ferromagnetic metallic ground state with $T_C \sim T_{MI} = 190–200$ K for nearly relaxed LPCMO films grown on LAO buffer with thickness $d_{LAO} = 7–23$ nm. For the thicker buffer layer ($d_{LAO} = 27$ nm) its out-of-plane lattice constant ($c_{LAO} \sim 0.3782$ nm) approaches the bulk value of the LAO and T_C of the LPCMO film decreases down to 184 K (see also Fig. 1b).

We have applied HAADF-STEM and iDPC-TEM techniques with atomic resolution in order to analyze the structure of the LPCMO films and relevant interfaces with the main aim of searching for a structural control parameter responsible for the very different magnetotransport behavior in the strained (on STO) and relaxed (on LAO/STO) LPCMO films. As one can see in Figs. 4 and 5 the respective LPCMO/STO and LPCMO/LAO/STO interfaces are atomically smooth and flat, evidencing that the LPCMO films have been coherently heteroepitaxially grown on the STO and on the LAO/STO substrates. On STO a homogeneous microstructure of a tetragonally distorted LPCMO film due to coherent tensile stress is present (see Fig. 4a). In contrast, the relaxed LPCMO/LAO/STO film reveals twinning domains seen in Fig. 5a with a lateral size of ≈ 30–80 nm. Bright regions represent LPCMO domains where the coherent scattering intensity indicates the b-axis oriented out-of-plane of the thin film, while dark regions correspond to LPCMO domains with b-axis in in-plane direction (either within the image plane or along the projection direction). This kind of microstructure has been previously observed for relatively thick ≈70 nm and relaxed LPCMO/MgO films with bulk-like magnetotransport indicating their orthorhombic Pnma structure[19]. Moreover, at the LAO/STO interface (Fig. 5a and b) one can clearly see an array of misfit dislocations resulting in a partial relaxation of the LAO buffer. The dislocations are irregularly spaced since strain relaxation may also occur along the perpendicular in-plane direction or via mixed defects in the case of a surface step on the STO. As a result, the in-plane lattice constant of the 10 nm thick LAO at the LPCMO/LAO interfaces decreases down to a = 0.385–0.386 nm (see Fig. 2c), thus, yielding a perfect lattice match to the LPCMO film.

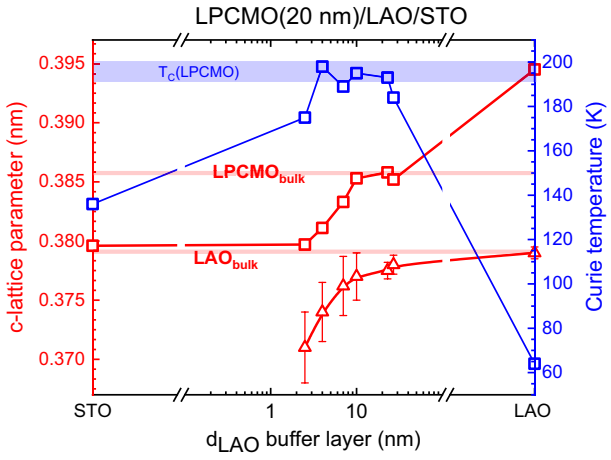

Figure 3. Correlation between the c-lattice parameters (red squares) and Curie temperatures of 20 nm thick LPCMO films grown on the LAO buffer layers versus logarithmic thickness in the range $d_{LAO} = 2.5 \div 27$ nm as well as grown directly on the STO(100) and LAO(100) substrates. C-lattice parameters of the LAO buffers/substrate are shown by red triangles.

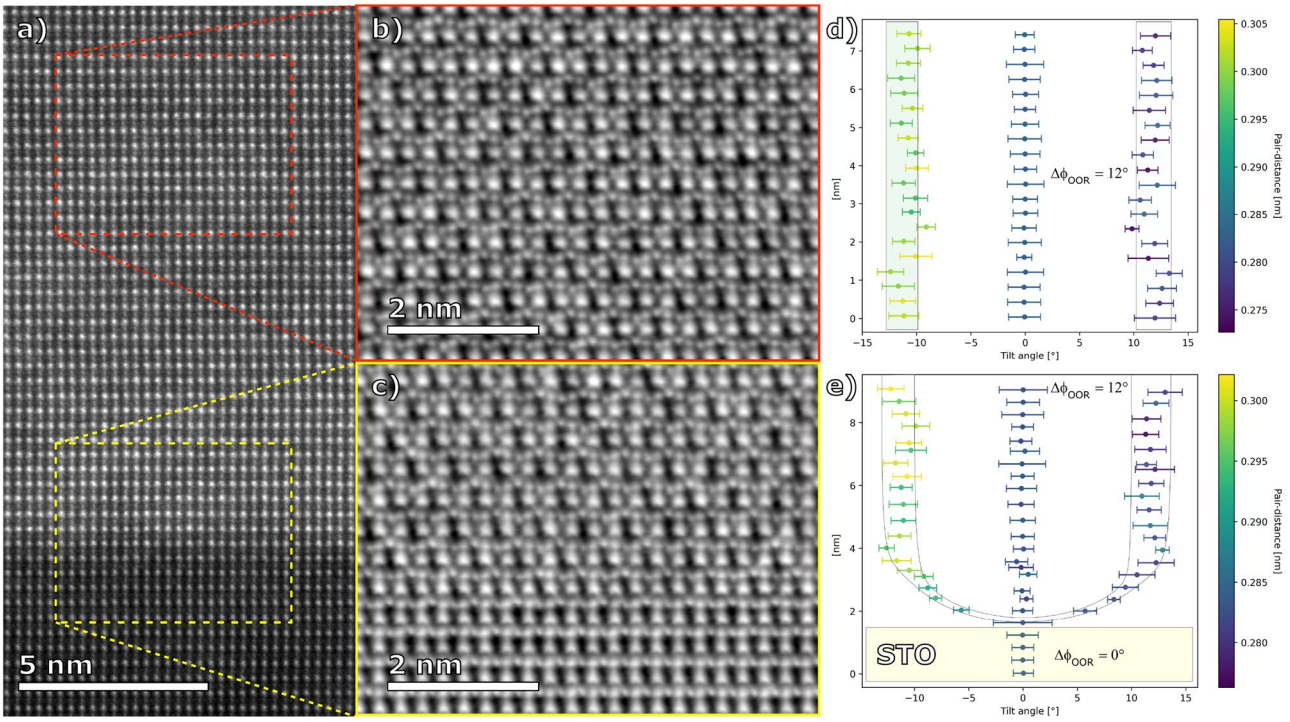

Figure 4. HAADF STEM (**a**) and iDPC-STEM (**b**, **c**) images of LPCMO films grown directly on STO substrate and corresponding statistical distribution evaluation of the oxygen octahedral rotation angles $\Delta\varphi_{OOR}$ (**d**, **e**) within each layer along the growth direction.

A remarkable difference between the tensile strained and relaxed LPCMO films on STO and LAO/STO substrates, respectively, was observed in iDPC-STEM images taken along the [110] zone axis as also shown in Figs. 4 and 6. The iDPC-STEM technique allows visualization of oxygen atoms[43], and thus to evaluate the Mn–O–Mn tilt/rotation angle, φ_{OOR}, which is known to play a decisive role in controlling magnetism and electron transport in perovskite manganites[10]. Note that, the aberration-corrected iDPC technique is able to determine oxygen positions with a pm precision.[44] The (Mn–O–Mn) bond angles have been evaluated within the plane of zone axis projection in terms of statistics of the bond angle deviation $\Delta\varphi = 0.5^*(180° - \varphi_{OOR})$, resolved as a function of the atomic layer number counted along the growth direction. The developed procedure is described in detail in SM[41] and histograms, obtained from the selected atomic layers within LPCMO films on STO and LAO/STO substrates are shown in Figs. 4d,e and 6d, respectively. One can see in Fig. 4 that an iDPC image of LPCMO/STO film reveals a homogeneous distribution of the Mn–O–Mn angle deviations within the volume of the LPCMO film (see Fig. 4b and d) with $\Delta\varphi_{OOR} \approx 12° \pm 1.5°$, from which an octahedral rotation/tilt angle $\varphi_{OOR} \approx 156°$ was obtained. Moreover, within the first 5–6 u.c of the LPCMO close to the LPCMO/STO interface the angle deviation smoothly changes from $\Delta\varphi = 0°$ characteristic for the cubic STO to that seen in the body of LPCMO film.

The HAADF-STEM and the corresponding iDPC-STEM images of LPCMO/LAO/STO film shown in Fig. 6 reveal excellent epitaxial growth as well as the change in $\Delta\varphi_{OOR}$ within the image projection. Moreover, they indicate that the STO-LAO interface is strained, and the oxygen rotation angle within the LPCMO layer also varies depending on the distance from the surface or LAO-LPCMO interface (see Fig. 6d). The LPCMO film is quantified by significantly smaller Mn–O–Mn angle deviations $\Delta\varphi \approx 7° \pm 2°$ and by the correspondingly larger octahedral tilt/rotation angle $\varphi_{OOR} \approx 166°$. However, the average angle deviations $\Delta\varphi$ are slightly larger at the LAO-LPCMO interface, while also being more disordered as indicated by the error bars (standard deviation of measurements within one cluster of data points). Note that, due to the presence of twining domains within the LPCMO/LAO/STO film the characteristic zig-zag pattern of φ_{OOR} can only be seen within one domain. Remarkably, both "strained" LPCMO/STO (Fig. 4) and "relaxed" LPCMO/LAO/STO (Fig. 6) interfaces appear sharp not only in the HAADF-STEM but also in the iDPC images. Indeed, the φ_{OOR} angle changes almost abruptly (within 1 u.c.) in case of the "relaxed" LPCMO/LAO/STO interface and within 5–6 u.c. for the "strained" LPCMO/STO one. This is in clear contrast to a much smoother behaviour observed at the $La_{0.7}Sr_{0.3}MnO_3$/STO interfaces in the films grown by pulsed laser deposition[45]: here the $\Delta\varphi$ acquires its natural value of ~ 7° or $\varphi_{OOR} \approx 166°$ after overcoming a transition zone with a thickness of about 15 u.c.

Discussion

A drastic difference in the magnetotransport of strained LPCMO/STO(100) and strain-engineered relaxed LPCMO/LAO/STO films has been observed. Namely, the former are insulating and poorly magnetic, whereas the latter possess ferromagnetic metallic ground state similar to that in bulk LPCMO. Furthermore, the smaller and larger octahedral tilt/rotation angles, i.e. $\varphi_{OOR} = 156°$ and 166°, were determined in strained and relaxed

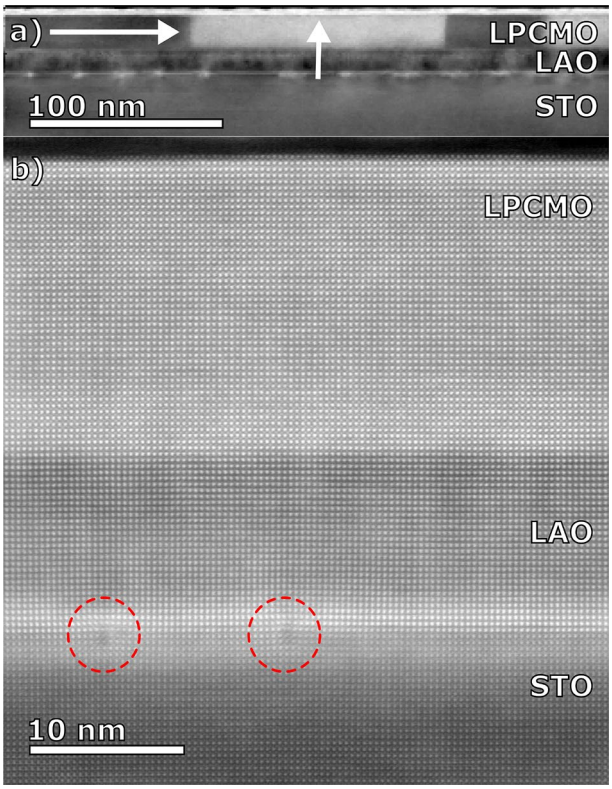

Figure 5. STEM evaluation of LPCMO(20 nm)/LAO(10 nm)/STO(100. (**a**) Orientation mapping of the LPCMO crystallographic b-axis by 4DSTEM nano-diffraction analysis, recorded in STO [100] zone axis orientation; (**b**) ADF-STEM image of the same sample in STO [100] orientation, where edge-type misfit dislocations between STO and LAO are visible when the dislocation line is parallel to the viewing direction, as highlighted by the dashed circles.

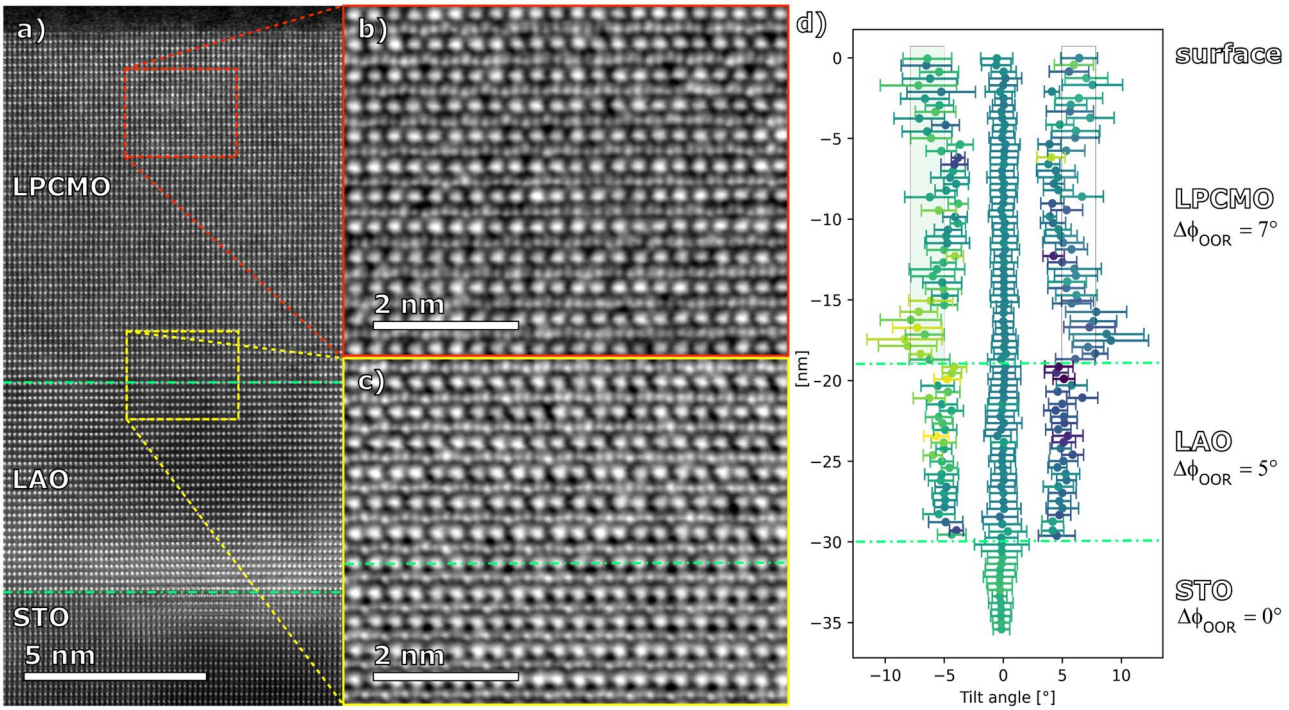

Figure 6. (**a**) HAADF-STEM overview in STO [110] zone axis. Corresponding iDPC-STEM data from selected regions within the LPCMO layer (**b**) and at the LPCMO-LAO interface (**c**). Quantification of $\Delta\varphi_{OOR}$ across the entire layer stack (**d**).

films, respectively. The reason for such differences seems to be a strong tetragonal lattice distortion in the tensile strained LPCMO/STO and its absence in the strain-engineered relaxed LPCMO/LAO/STO. It is likely that tetragonal distortion, reducing the c-lattice parameter down to c = 0.3796 nm (see Fig. SM-1, ref.[41]) and keeping in-plane a- and b-lattice parameters of LPCMO equal to that of the STO due to epitaxy (see Fig. 2), causes a strong decrease of the rotation/tilt angle down to a value even smaller than in the bulk LPCMO.

According to classical neutron diffraction study by Radaelli et al.[10], the optimally doped A-site substituted bulk manganites with general formula $(A_{1-y}A'_y)_{0.7}A''_{0.3}MnO_3$ (A, A' = La, Pr; A'' = Ca, Sr, Ba) possess different φ_{OOR} (or Mn–O–Mn) angles controlled by the average radius of the A-site cation $\langle R_A \rangle$. The φ_{OOR} increases with increasing $\langle R_A \rangle$ reflecting the tendency to change crystal structure from the orthorhombic (Pnma) structure for small radii $\langle R_A \rangle \leq 0.124$ nm and small Mn–O-Mn angles $156° < \varphi_{OOR} < 164°$ to the rhombohedral (R-3c) one for larger $\langle R_A \rangle > 0.124$ nm and larger angles $165° < \varphi_{OOR} < 171°$. The here studied LPCMO material in the bulk form with small $\langle R_A \rangle = 0.1195$ possesses small $\varphi_{OOR} = 159°$ and belongs to an orthorhombic structure[10]. Thus, the observed reduction of the Mn–O–Mn angle for strained LPCMO/STO film down to $\varphi_{OOR} \approx 156°$, which is even smaller than that in bulk LPCMO, is a result of tensile strain and tetragonal distortion. Note that a similarly small $\varphi_{OOR} \approx 156°$ has been determined[10] for bulk $Pr_{0.7}Ca_{0.3}MnO_3$ (PCMO) with a smaller $\langle R_A \rangle = 0.11793$ nm, the ground state of which is known to be an antiferromagnetic insulator[46]. A close similarity with the observed insulating and weakly magnetic ground state of the coherently strained LPCMO/STO film is worth to note. Taken all together this nicely demonstrates correlations, on one hand, between the structure/chemical pressure and magnetism, and, on the other hand, between the epitaxy pressure (stress) and a unique structural parameter φ_{OOR} in the LPCMO films.

Moreover, we have experimentally determined that the mechanism underlying strain relaxation of the LAO buffer grown on STO substrate, having large lattice misfit of 3%, is an abrupt octahedral decoupling at the LAO/STO interface (see Fig. 6) favored by formation of misfit dislocations (see Fig. 5). As a result, the octahedral tilt/rotation angle in the LAO decreases and the in-plane lattice parameter of the partially relaxed LAO increases. Thus, for the thickness $d_{LAO} = 7–10$ nm one obtains a perfect lattice and angle matching to the LPCMO. Together with the mutual LPCMO/LAO elastic adjustment at the interface, as both layers are of comparable thickness of 10–20 nm, this provides a perfect LPCMO/LAO epitaxy. The observed large $\varphi_{OOR} = 166°$ in the relaxed LPCMO/LAO/STO film is inherited from the rhombohedral LAO buffer layer which also shows large $\varphi_{OOR} \approx 170°$ (see Fig. 5f) close to the $\varphi_{OOR} \approx 169°$ in bulk LAO[42]. Note, that the relaxed LPCMO/LAO/STO film still remains in its natural orthorhombic structure as indicated by the twinning domains in the HAADF-STEM (see Fig. 5a) which originate from different a- and b-lattice parameters inherent to the orthorhombic structure. The same twinning domain structure has been observed earlier in the relaxed LPCMO/MgO films[19].

The improvement of magnetotransport in very thin relaxed LPCMO films is interpreted within the well-known orbital mechanisms controlling magnetism in manganites[47]. First, *orbital disorder*, i.e. no preferred orbital occupation of Mn(3d) orbitals in the relaxed film, as the tetragonal distortion is missing. Second, improved/enhanced Mn(3d)–O(2p) *orbital hybridization* as the Mn–O–Mn bonds are significantly straightened. Third, the resulting enhancement of *double exchange interaction*[48–50] stabilizes ferromagnetic metallic ground state of the LPCMO/LAO/STO thin films. The fundamentally important structural control parameter[20], i.e. octahedral tilt/rotation angle was found to be surprisingly large ($\varphi_{OOR} = 166°$) in the strain-engineered and relaxed LPCMO/LAO/STO film. In contrast, the strong tetragonal distortion in the strained LPCMO/STO with small $\varphi_{OOR} = 156°$ leads to an orbital reconstruction with $3dMn_{(x2-y2)}$ orbitals being more populated[51] and an enhancement of antiferromagnetic superexchange interaction, which as well favors insulating behavior[47,52]. Thus, we believe our findings could open a promising and relatively simple way to control the colossal magnetoresistive LPCMO films in a wide range of properties by strain-engineered control of octahedral tilt/rotation angle. Namely, by tuning the thickness of the LAO buffer on STO substrate one creates the opportunity not only to grow the relaxed films with bulk-like properties for $d_{LAO} = 10–20$ nm, but also the tensile ($0 < d_{LAO} < 7$ nm) and compressively ($d_{LAO} > 30$ nm) strained films. Such LPCMO films with controllable strain state could be of interest for further studies of CMR physics in perovskite manganites.

Conclusions

Strain-engineering of thin hetero-epitaxial LPCMO films beyond substrate limitations has been realized within a metalorganic aerosol deposition technique by tuning the thickness of the LAO-buffer on STO(100) substrates. For 7–20 nm thick LAO buffer layers the strain-free LPCMO films with thickness d = 10–20 nm and bulk magnetotransport properties have been obtained. The octahedral tilt/rotation Mn–O–Mn angles, determined by iDPC-STEM, were shown to be very sensitive to the epitaxy strain as a tensile strained LPCMO/STO film shows a reduced $\varphi_{OOR} \approx 156°$. This is shown to be the main reason of the suppressed ferromagnetism and insulating behaviour for strained LPCMO films. A significantly increased $\varphi_{OOR} \approx 166°$ for the strain-free LPCMO/LAO/STO film results in an enhancement of double exchange interaction, yielding the optimized ferromagnetic metallic behaviour.

Data availability

The datasets used and/or analyzed during the current study available from the corresponding author on reasonable request.

Received: 29 November 2023; Accepted: 4 February 2024
Published online: 08 February 2024

References

1. Goodenough, J. B. Electronic and ionic transport properties and other physical aspects of perovskites. *Rep. Prog. Phys.* **67**, 1915 (2004).
2. Arulraj, A., Dinnebier, R. E., Carlson, S., Hanfland, M. & van Smaalen, S. Strain effects in perovskite manganites. *Prog. Solid State Chem.* **35**, 367 (2007).
3. Hu, S. *et al.* Substrate-dependent post-annealing effects on the strain state and electrical transport of epitaxial $La_{5/8-y}Pr_yCa_{3/8}MnO_3$ films. *AIP Adv.* **4**, 067109 (2014).
4. Millis, A. J. Lattice effects in magnetoresistive manganese perovskites. *Nature* **392**, 147 (1998).
5. Tokura, Y. & Nagaosa, N. Orbital physics. *Science* **288**, 462 (2000).
6. Dagotto, E. & Tokura, Y. Strongly correlated electronic materials: Present and future. *MRS Bull.* **33**, 1037 (2008).
7. Kwon, C. *et al.* Stress-induced effects in epitaxial $La_{0.7}Sr_{0.3}MnO_3$ films. *J. Magn. Magn. Mater.* **172**, 22923 (1997).
8. Singh, S., Tyagi, P. K. & Singh, H. K. Structure, magnetism and electrical transport in epitaxial $La_{0.23}Pr_{0.41}Ca_{0.36}MnO_3$ thin films: Consequences of film thickness. *AIP Adv.* **8**, 095002 (2018).
9. Uehara, M., Mori, S., Chen, C. H. & Cheong, S.-W. Percolative phase separation underlies colossal magnetoresistance in mixed-valent manganites. *Nature (London)* **399**, 560 (1999).
10. Radaelli, P. G. *et al.* Structural effects on the magnetic and transport properties of perovskite $A_{1-x}A'_xMnO_3$ (x = 0.25 and 0.30). *Phys. Rev. B* **56**, 8265 (1997).
11. Moshnyaga, V. & Samwer, K. Electron-lattice correlations and phase transitions in CMR manganites. *Ann. Phys. (Berlin)* **523**, 652 (2011).
12. Seick, C. *et al.* Energy relaxation in $(La_{0.6}Pr_{0.4})_{0.7}Ca_{0.3}MnO_3$ films across the metal-insulator transition. *Phys. Rev. B* **107**, 085115 (2023).
13. Bruchmann-Bamberg, V. *et al.* Magnetism and thermal transport of exchange-spring-coupled $La_{2/3}Sr_{1/3}MnO_3/La_2MnCoO_6$ superlattices with perpendicular magnetic anisotropy. *Nanomaterials* **13**, 2897 (2023).
14. Meyer, T. L., Jiang, L., Park, S., Egami, T. & Lee, H. N. Strain-relaxation and critical thickness of epitaxial $La_{1.85}Sr_{0.15}CuO_4$ films. *APL Mater.* **3**, 126102 (2015).
15. Ranno, L., Llobert, A., Tiron, R. & Favre-Nicolin, E. Strain-induced magnetic anisotropy in epitaxial manganite films. *Appl. Surf. Sci.* **188**, 170 (2002).
16. Gazquez, J. *et al.* Lattice mismatch accommodation via oxygen vacancy ordering in epitaxial $La_{0.5}Sr_{0.5}CoO_{3-\delta}$ thin films. *APL Mater.* **1**, 012105 (2013).
17. Narayan, J. & Larson, B. C. Domain epitaxy: A unified paradigm for thin film growth. *J. Appl. Phys.* **93**, 278 (2003).
18. Moshnyaga, V. *et al. A*-Site ordering versus electronic inhomogeneity in colossally magnetoresistive manganite films. *Phys. Rev. Lett.* **97**, 107205 (2006).
19. Moshnyaga, V. *et al.* Intrinsic antiferromagnetic coupling underlies colossal magnetoresistance effect: Role of correlated polarons. *Phys. Rev. B* **89**, 024420 (2014).
20. Li, W., Shi, J., Zhang, K. H. L. & MacManus-Driscoll, J. L. Defects in complex oxide thin films for electronics and energy applications: Challenges and opportunities. *Mater. Horizons* **7**, 2832 (2020).
21. Dhole, S., Chen, A., Nie, W., Park, B. & Jia, Q. Strain engineering: A pathway for tunable functionalities of perovskite metal oxide films. *Nanomaterials* **12**, 835 (2022).
22. Si, W. & Xi, X. X. Epitaxial-strain-induced insulator-superconductor transition in undoped and lightly doped $La_2CuO_{4+\delta}$. *Appl. Phys. Lett.* **78**, 240–242 (2001).
23. Xi, X. & Si, W. Buffer layer engineering for $La_{2-x}Sr_xcuO_4$ films. *Phys. C* **341–348**, 665–666 (2000).
24. Oh, J.-Y., Ko, Y.-J., Yang, D.-S., Jeong, W. & Kang, B. Strain engineering using $La_{0.7}Sr_{0.3}MnO_3$ buffer layer for enhancing superconductivity in $GdBa_2Cu_3O_{7-x}$ films. *J. Mater. Sci. Mater. Electron.* **33**, 15272 (2022).
25. Huang, Z. *et al.* Tuning the ground state of $La_{0.67}Ca_{0.33}MnO_3$ films via coherent growth on orthorhombic $NdGaO_3$ substrates with different orientations. *Phys. Rev. B* **86**, 014410 (2012).
26. Zhang, W. *et al.* Epitaxial-strain–dependent reorientation of oxygen octahedral tilting axis in manganite films. *Europ. Phys. Lett.* **137**, 36002 (2022).
27. Jin, F. *et al.* Uniaxial strain-controlled ground states in manganite films. *Nano Lett.* **20**, 1131 (2020).
28. Liu, J. *et al.* Controlled properties of perovskite oxide films by engineering oxygen octahedral rotation. *JUSTC* **53**, 1 (2023).
29. Li, W. *et al.* Atomic-scale control of electronic structure and ferromagnetic insulating state in perovskite oxide superlattices by long-range tuning of BO_6 octahedra. *Adv. Funct. Mater.* **30**, 2001984 (2020).
30. Li, D. *et al.* Manipulating the metal-to-insulator transition and magnetic properties in manganite thin films via epitaxial strain. *Phys. Rev. B* **105**, 165426 (2022).
31. Han, H. *et al.* Interfacial oxygen octahedral coupling-driven robust ferroelectricity in epitaxial $Na_{0.5}Bi_{0.5}TiO_3$ thin films. *Research* **6**, 0191 (2023).
32. Zhang, Z. *et al.* Tuning the magnetic anisotropy of $La_{0.67}Sr_{0.33}MnO_3$ by $CaTiO_3$ spacer layer on the platform of $SrTiO_3$. *J. Magn. Magn. Mater.* **554**, 169299 (2022).
33. Shao, P.-W. & Chu, Y.-H. Advances in strain engineering on oxide heteroepitaxy. *Matter* **4**, 2117–2119 (2021).
34. Lu, D. *et al.* Strain tuning in complex oxide epitaxial films using an ultrathin strontium aluminate buffer layer. *Phys. Status Solidi RRL* **12**, 1700339 (2018).
35. Deng, X. *et al.* Strain engineering of epitaxial oxide heterostructures beyond substrate limitations. *Matter* **4**, 1323 (2021).
36. Hoffmann-Urlaub, S. *et al.* Tailoring c-axis orientation in epitaxial Ruddlesden-Popper $Pr_{0.5}Ca_{1.5}MnO_4$ films. *Adv. Mater. Interfaces* **8**, 2002049 (2021).
37. Kajimoto, R. *et al.* Hole-concentration-induced transformation of the magnetic and orbital structures in $Nd_{1-x}Sr_xMnO_3$. *Phys. Rev. B* **60**, 9506 (1999).
38. Ohtomo, A. & Hwang, H. Y. A high-mobility electron gas at the $LaAlO_3/SrTiO_3$ heterointerface. *Nature* **427**, 423 (2004).
39. Jungbauer, M. *et al.* Atomic layer epitaxy of Ruddlesden-Popper $SrO(SrTiO_3)_n$ films by means of metalorganic aerosol deposition. *Appl. Phys. Lett.* **105**, 251603 (2014).
40. Kawasaki, M. *et al.* Atomic control of the $SrTiO_3$ crystal surface. *Science* **266**, 1540 (1994).
41. Supplementary Information on the morphology, structure, determination of Curie temperature and evaluation procedure of octahedral tilt angles is available at https://doi.org/10.1038/s41598-024-53722-9.
42. Miiller, K. A., Berlinger, W. & Waldner, F. Characteristic structural phase transition in perovskite- type compounds. *Phys. Rev. Lett.* **21**, 814 (1968).
43. Lazić, I., Bosch, E. G. T. & Lazar, S. Phase contrast STEM for thin samples: Integrated differential phase contrast. *Ultramicroscopy* **160**, 265 (2016).
44. Gauquelin, N. *et al.* Determining oxygen relaxations at an interface: A comparative study between transmission electron microscopy techniques. *Ultramicroscopy* **181**, 178 (2017).
45. Li, Z. *et al.* Competing interfacial reconstruction mechanisms in $La_{0.7}Sr_{0.3}MnO_3/SrTiO_3$ heterostructures. *ACS Appl. Mater. Interfaces* **8**, 24192 (2016).

46. Tomioka, Y., Asamitsu, A., Kuwahara, H., Moritomo, Y. & Tokura, Y. Magnetic-field-induced metal-insulator phenomena in $Pr_{1-x}Ca_xMnO_3$ with controlled charge-ordering instability. *Phys. Rev B* **53**, R1689 (1996).
47. Tokura, Y. & Nagaosa, N. Orbital physics in transition-metal oxides. *Science* **288**, 462 (2000).
48. Zener, C. Interaction between the d-shells in the transition metals. II. Ferromagnetic compounds of manganese with perovskite structure. *Phys. Rev.* **82**, 403 (1951).
49. Anderson, P. W. & Hasegawa, H. Considerations on double exchange. *Phys. Rev.* **100**, 675 (1955).
50. de Gennes, P.-G. Effects of double exchange in magnetic crystals. *Phys. Rev.* **118**, 141 (1960).
51. Pesquera, D. *et al.* Surface symmetry-breaking and strain effects on orbital occupancy in transition metal perovskite epitaxial films. *Nat. Commun.* **3**, 1189 (2012).
52. Fang, Z., Solovyev, I. V. & Terakura, K. Phase diagram of tetragonal manganites. *Phys. Rev. Lett.* **84**, 3169 (2000).

Acknowledgements

This work was financially supported by the DFG via SFB 1073 (TP Z02). V.R. acknowledges the European Regional Development Fund and the State of Brandenburg for the Themis Z TEM (part of the Potsdam Imaging and Spectral Analysis Facility (PISA)).

Author contributions

P.H., K.P.S. & V.B.B. prepared and characterized (structure, magnetism and transport) the films. R.G., and P.G. carried out and characterized reciprocal space mapping. U.R., V.R. & M.S. carried out and evaluated TEM measurements. V.M. supervized the project and wrote original darft of the manuscript. All authors reviewed the manuscript.

Funding

Open Access funding enabled and organized by Projekt DEAL.

Competing interests

The authors declare no competing interests.

Additional information

Supplementary Information The online version contains supplementary material available at https://doi.org/10.1038/s41598-024-53722-9.

Correspondence and requests for materials should be addressed to V.M.